RSC Advances

PAPER

View Article Online
View Journal | View Issue

Cite this: *RSC Adv.*, 2020, **10**, 8244

Improving the corrosion resistance of micro-arc oxidation coated Mg–Zn–Ca alloy

Yang Chen,[ab] Jinhe Dou,[b] Zengfen Pang,[c] Huijun Yu,*[a] Chuanzhong Chen *[b] and Jinkui Feng *[b]

Received 20th December 2019
Accepted 11th February 2020

DOI: 10.1039/c9ra10741j

rsc.li/rsc-advances

Four additives (Na_2WO_4, nano-hydroxyapatite, K_2TiF_6 and NaF) were added into the $Na_5P_3O_{10}$ + NaOH + $C_3H_8O_3$ base electrolyte according to the orthogonal design of four factors three levels (L_9 (3^4)). Nine different micro-arc oxidation (MAO) coatings were fabricated on Mg–2Zn–0.5Ca alloys through orthogonal experiments. The effects of four additives on the microstructure, mechanical properties, corrosion resistance and biocompatibility of MAO coatings were investigated through X-ray diffraction (XRD), scanning electron microscopy (SEM) with energy dispersive X-ray spectroscopy (EDS), electrochemical corrosion test and *in vitro* degradation test. The addition of nano-hydroxyapatite and K_2TiF_6 showed self-sealing effects and contributed to the corrosion resistance of the samples significantly. The addition of 0.5 g L^{-1} Na_2WO_4 markedly elevated the bonding strength of the coatings with the substrate. The optimal combination of factors and levels considering both mechanical properties and corrosion resistance was: 0.5 g L^{-1} Na_2WO_4, 0 g L^{-1} NaF, 5 g L^{-1} n-HAp, 5 g L^{-1} K_2TiF_6. The growth mechanism of MAO coatings combining with the visual phenomenon was discussed as well.

1 Introduction

Magnesium alloys have drawn extensive attention as biodegradable orthopedic implant materials in recent years. Magnesium alloys possess low specific density (1.74–1.84 g cm^{-3}) and Young's modulus (41–45 GPa) close to those of natural bone tissues (1.8–2.1 g cm^{-3}, 15–25 GPa).[1] Magnesium naturally exists in bone tissues and its corrosion products generated *in vivo* can be easily excreted by human bodies.[2,3] Furthermore, magnesium alloys avert a second surgery of removing the implant and relieve the patients' pain compared to conventional permanent metallic biomaterials (*e.g.* stainless steels, titanium alloys, cobalt chromium alloys, *etc.*).[4] However, the widespread use of magnesium alloys for biomedical applications is still limited due to its rapid biodegradation rate when exposed to the physiological environment,[5,6] thereby losing mechanical integrity before the host tissues sufficiently heal.[7,8] Furthermore, the large amount of hydrogen gas generated from the degradation of implants is not conducive to the tissue healing process. The shifting pH values are pernicious to cell viability.[9]

The addition of alloying elements can improve mechanical properties and corrosion resistance of pure magnesium.[10] The alloying elements must be nontoxic and safe to human bodies.[11] The addition of zinc (Zn) element helps to improve the mechanical properties of magnesium alloy by grain refining.[12] In addition, Zn element promotes bone formation, whilst inhibits bone resorption.[13,14] Therefore, Zn is chosen as the alloying element of magnesium alloys due to its biocompatibility, osteogenic activity, antibacterial ability and grain refining effect.[15,16] Calcium (Ca) is a biocompatible element owing to its natural existence in bones.[17] And the calcium addition elevates the corrosion resistance of magnesium alloys in chloride containing solutions.[18] Based on previous studies and experiments,[19–21] we chose Mg–2Zn–0.5Ca alloys as our substrate metal.

Numerous surface treatments have been elaborated to improve the corrosion properties and biocompatibility of magnesium based alloys, such as chemical conversion coating, electrochemical treatment, organic coating and micro-arc oxidation (MAO).[22–24] Micro-arc oxidation is an environment friendly technique to prepare uniform coatings with excellent adhesion and corrosion resistance.[25,26] The micro-pores formed in the MAO coatings could contribute to the growth of bone tissues.[27] The nature of substrate metals, composition and concentration of electrolyte, and applied electrical parameters plays a crucial role in the properties of coatings.[28–31] The composition of electrolytes can change the properties of

[a]*Key Laboratory of High-efficiency and Clean Mechanical Manufacture (Ministry of Education), National Demonstration Center for Experimental Mechanical Engineering Education, School of Mechanical Engineering, Shandong University, Ji'nan 250061, China. E-mail: yhj2001@sdu.edu.cn*

[b]*Key Laboratory for Liquid-Solid Structural Evolution and Processing of Materials, Ministry of Education, Shandong Engineering Research Center for Superhard Materials, School of Materials Science and Engineering, Shandong University, Ji'nan 250061, Shandong, China. E-mail: czchen@sdu.edu.cn; jinkui@sdu.edu.cn*

[c]*Shandong Tumor Hospital and Institute, Ji'nan 250117, Shandong, P. R. China*

coatings significantly by altering the microstructure and composition of the coating. The addition of sodium tungstate (Na_2WO_4) increases the electrolytic conductivity and enlarges the size of micro-pores generated in MAO coatings on AZ91HP magnesium alloys.[32] Hydroxyapatite (HA, $Ca_{10}(PO_4)_6(OH)_2$) is the major mineral component of bone and teeth.[33] Therefore, HA is a promising candidate for preparing coatings on magnesium alloys in terms of its outstanding biocompatibility, bioactivity and corrosion resistance.[34,35] NaF additives decrease the energy consumption of MAO process and contribute to the growth of the coating. The addition of K_2TiF_6 in the electrolytes helps to seal the micro-pores and improve the corrosion resistance of MAO coatings.[36–38] Moreover, F^- participates in the arc discharge during the micro-arc oxidation process and forms dense ceramic containing MgF_2.[39]

In this paper, we chose sodium tripolyphosphate ($Na_5P_3O_{10}$), sodium hydroxide (NaOH) and glycerine ($C_3H_8O_3$) as our base electrolyte. Na_2WO_4, nano-hydroxyapatite, K_2TiF_6 and NaF was added as extra additives. Nine different ceramic coatings were fabricated on Mg–2Zn–0.5Ca alloys by orthogonal design of four factors three levels to optimize the electrolyte solution. The microstructure, phase and elemental composition, corrosion resistance, biocompatibility of these samples were discussed.

2 Experimental

2.1 Materials and coating preparation

Mg–2Zn–0.5Ca alloy was cast using commercial purity Mg (99.99%), Zn blocks (99.99%) and Mg–20Ca master alloys. The ingot was cut into rectangular specimens with size of 10 mm × 10 mm × 12 mm. Prior to the MAO treatment, every sample was ground with SiC papers up to 1000 grit, rinsed with distilled water, degreased with acetone and dried with a blower. The base electrolyte contained 10 g L^{-1} $Na_5P_3O_{10}$ + 2 g L^{-1} NaOH + 10 mL L^{-1} $C_3H_8O_3$ in distilled water. Four additives Na_2WO_4, nano-hydroxyapatite (n-HAp), K_2TiF_6 and NaF were added into the base electrolyte according to orthogonal design of four factors three levels (as shown in Table 1). The specimens were numbered A1–A9 in terms of different combination of additives. All solutions were prepared using analytical grade reagents and distilled water. The MAO treatment was performed using a constant pressure control mode. During the MAO process, the applied positive voltage, pulse frequency, applied negative voltage, positive duty ratio, negative duty ratio and ratio of positive and negative pulses were 350 V, 600 HZ, 30 V, 30%, 20%, 1 : 1 respectively. The oxidation process was carried out for 10 min under 30 °C.

2.2 Coating characterization

The thickness of MAO coatings was measured by MiniTest 600B FN2 microprocessor coating thickness gauge (Elektrophysik Koln). The final value obtained was the average value of six replicate measurements. WS-20004 Scratch Tester was used to evaluate the adhesion strength of MAO coatings. The morphology and element distribution was investigated using scanning electron microscopes (SEM, Hitachi S-3400N) combined with energy dispersive spectrum (EDS, Horiba EMAX X-act). The phase composition of the coatings before and after immersion was detected using X-ray diffractometer (SHIMADZU XRD-6100) with Cu-K_α radiation at a scanning speed of 4° min^{-1}.

Table 1 The composition and concentration of extra additives by orthogonal design

Sample codes	Additives			
	Na_2WO_4 (g L^{-1})	NaF (g L^{-1})	n-HAp (g L^{-1})	K_2TiF_6 (g L^{-1})
A1	—	—	—	—
A2	—	2.5	5.0	5.0
A3	—	5.0	10.0	10.0
A4	0.5	—	5.0	10.0
A5	0.5	2.5	10.0	—
A6	0.5	5.0	—	5.0
A7	1.0	—	10.0	5.0
A8	1.0	2.5	—	10.0
A9	1.0	5.0	5.0	—

2.3 Electrochemical corrosion test

Electrochemical behavior of MAO treated samples and bare Mg alloy substrate was studied in simulated body fluid (SBF). The SBF was prepared by dissolving the analytical grade reagents following the sequence of NaCl, $NaHCO_3$, KCl, $K_2HPO_4 \cdot 3H_2O$, $MgCl_2 \cdot 6H_2O$, 1.0 mol L^{-1} HCl, $CaCl_2$, Na_2SO_4 and tris(hydroxymethyl)aminomethane ($(CH_2OH)_3CNH_2$) in distilled water at 36.5 ± 0.5 °C. The pH was adjusted to 7.2–7.3 with 1.0 mol L^{-1} HCl. A conventional three electrode electrochemical cell was employed to assess the electrochemical behavior, which contained a platinum wire counter electrode, a saturated calomel reference electrode, and one 10 mm × 10 mm side of specimen as the working electrode. Potentiodynamic polarization tests were performed at a scan rate of 1 mV s^{-1} from −2500 mV to 1000 mV.

2.4 *In vitro* degradation test

The MAO treated samples and bare Mg alloy substrate was immersed in SBF for 28 days. Each sample was submerged in 45 mL SBF separately, and three parallel samples were evaluated to minimize contingency. The ratio of the samples' surface area to SBF volume is 8 mm^2 : 1 mL. The SBF was renewed every the other day to keep it fresh and stable whilst avoiding sediment during the immersion process. The pH values were tested and recorded every the other day to evaluate the degradation stability by pH meter. The samples were picked out from the SBF after the immersion, cleaned in distilled water and dried in a drying oven.

3 Results and discussions

The addition of four additives in the electrolyte plays an important role in the microstructure, mechanical properties,

corrosion resistance and biocompatibility of MAO coated Mg–2Zn–0.5Ca alloys. The orthogonal experiment is an efficient and economical way to obtain the results. The four additives Na_2WO_4, NaF, n-HAp and K_2TiF_6 are defined as factors j (j = A, B, C, D respectively). Each factor possesses three levels i (i = 1, 2, 3), representing three different concentrations. k_{ji} is defined as the average value of the evaluation indexes of all levels i in each factor j, which is used to evaluate the optimal combination of factors and levels. R_j is the difference value between the maximum k_{ji} and minimum k_{ji}. R_j value is used for assessing the influence degree of the factors, a larger R_j value means a greater impact on the results.[40] The calculation methods of factor B is shown below:

$$k_{B1} = (Y_1 + Y_4 + Y_7)/3;$$

$$k_{B2} = (Y_2 + Y_5 + Y_8)/3;$$

$$k_{B3} = (Y_3 + Y_6 + Y_9)/3;$$

$$R_j = \max(k_{Bi}) - \min(k_{Bi}); \quad (1)$$

where k_{Bi} is the k value of factor B with i level; and Y_z (z = 1–9) is the value of evaluation indexes E_{corr} (V per SCE), I_{corr} (A cm^{-2}), W_l (%) and B_s (N) of nine samples respectively. Higher E_{corr} (V per SCE) value indicates the samples are harder to corrode while lower I_{corr} (A cm^{-2}) value means a slower corrosion rate. Meanwhile, lower W_l (%) value promises better corrosion resistance. Table 2 shows the visual analysis of the samples' corrosion potential (E_{corr} (V per SCE)), corrosion current density (I_{corr} (A cm^{-2})), weight loss percentage after 28 days' immersion (W_l (%)) and bonding strength (B_s (N)). As shown in the Table 2, the addition of Na_2WO_4 has a greater impact on the bonding strength of the samples, thus, the optimal addition of Na_2WO_4 is 0.5 g L^{-1}. Three evaluation indexes show that the best concentration of NaF is 0 g L^{-1}. Furthermore, the addition of 0 g L^{-1} and 5 g L^{-1} NaF leads to similar I_{corr} value. In consequence, the addition of 0 g L^{-1} NaF is the best choice. The addition of n-HAp influences greater on the I_{corr} (A cm^{-2}) of the samples and the optimal concentration is 5 g L^{-1}. The addition of K_2TiF_6 has obvious impact on the I_{corr} (A cm^{-2}), W_l (%) and B_s (N) of the samples. The concentration of 5 g L^{-1} K_2TiF_6 promises slow degradation rate as well as strong bonding strength. Therefore, the optimal combination of factors and levels is: 0.5 g L^{-1} Na_2WO_4, 0 g L^{-1} NaF, 5 g L^{-1} n-HAp and 5 g L^{-1} K_2TiF_6.

3.1 Coating appearance, thickness and bonding strength

The MAO coatings presented different degrees of white and blue color as the composition and concentration of the electrolyte solutions changed (as shown in Fig. 1). The samples without the addition of K_2TiF_6 (A1, A5, A9) all presented white color, thus, the addition of K_2TiF_6 led to the appearance of blue color. Moreover, as the concentration of K_2TiF_6 increased, the color of the coatings grew darker. Li *et al.*[41] proved that MgF_2 coating reflected red and blue light under the white light. The combination of different volume MgF_2 phases and Ti element on the coating surface presented various degrees of blue with different saturation *via* light scattering. The samples A2, A6, A7 showed light grey blue with the addition of 5 g L^{-1} K_2TiF_6, while samples A3, A4, A8 presented darker steel blue with more addition of 10 g L^{-1} K_2TiF_6.

The thickness and adhesion of nine different MAO coatings was shown in Fig. 2. The thickness of MAO coatings had no direct relations to the corrosion resistance of the samples. The corrosion properties of the samples mainly depended on the configuration and size of the defects (micro-pores and micro-cracks). The adhesion strength of MAO coatings to the substrate was crucial properties to identify the mechanical integrity of the samples, and it was closely related to the corrosion properties of MAO coated samples.[42] According to the range analysis of orthogonal experiments (as shown in Table 2),

Table 2 The visual analysis of corrosion potential (E_{corr} (V per SCE)), corrosion current density (I_{corr} (A cm^{-2})), weight loss percentage after 28 days' immersion (W_l (%)) and bonding strength (B_s (N)) of the samples

E_{corr} (V per SCE)	Na_2WO_4	NaF	n-HAp	K_2TiF_6	I_{corr} (A cm^{-2})	Na_2WO_4	NaF	n-HAp	K_2TiF_6
k_1	−1.588	−1.598	−1.658	−1.703	k_1	6.73×10^{-6}	7.32×10^{-6}	9.37×10^{-6}	1.69×10^{-5}
k_2	−1.713	−1.662	−1.671	−1.704	k_2	1.01×10^{-5}	1.24×10^{-5}	3.98×10^{-6}	4.16×10^{-6}
k_3	−1.692	−1.733	−1.664	−1.585	K_3	1.02×10^{-5}	7.31×10^{-6}	1.37×10^{-5}	5.99×10^{-6}
R_j	0.125	0.135	0.013	0.119	R_j	3.45×10^{-6}	5.1×10^{-6}	9.71×10^{-6}	1.27×10^{-5}
Sequence of factors	B > A > D > C					D > C > B > A			
Optimal combination	A_1	B_1	C_1	D_3		A_1	B_3	C_2	D_2
W_l (%)	Na_2WO_4	NaF	n-HAp	K_2TiF_6	B_s (N)	Na_2WO_4	NaF	n-HAp	K_2TiF_6
k_1	3.731	3.277	3.824	5.159	k_1	16.27	25.39	17.77	16.11
k_2	3.791	3.758	3.618	3.002	k_2	25.92	20.98	18.73	25.57
k_3	3.327	3.815	3.407	2.688	k_3	20.50	16.32	26.19	21.01
R_j	0.464	0.538	0.418	2.471	R_j	9.65	9.07	8.42	9.46
Sequence of factors	D > B > A > C					A > D > B > C			
Optimal combination	A_3	B_1	C_3	D_3		A_2	B_1	C_3	D_2

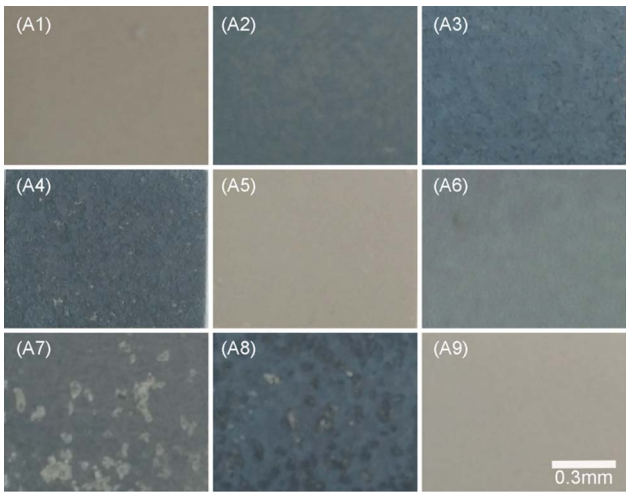

Fig. 1 Appearance of MAO coatings prepared by nine different electrolytes (samples A1–A9).

the addition of K_2TiF_6 and NaF influenced the thickness of the MAO coatings significantly. The addition of K_2TiF_6 could elevate the electrolyte conductivity and decrease the melting point of the components in the anode/electrolyte interface which lower the breakdown voltage.[43] Thus, the increase of K_2TiF_6 concentration improved the formation rate of the coatings and raised the thickness of the coatings evidently. The addition of 5 g L^{-1} K_2TiF_6 exhibited the best bonding strength. With the increase of NaF additives, the MAO coatings grew much thicker, but the adhesion of MAO coatings with the substrate decreased. The better bonding strength was more conducive to mechanical properties of MAO coatings, thus the addition of NaF was harmful to the samples. Na_2WO_4 additives possessed greater impact on the bonding strength of the samples than the others. And 0.5 g L^{-1} addition of Na_2WO_4 showed strongest bonding strength. The addition of n-HAp hardly had any effect on the thickness of the coatings, but the increase of n-HAp additives elevated the adhesion of MAO coatings to a big extent. Fig. 2 showed that there are no direct connections between the thickness and adhesion of MAO coatings. The samples A4 and A7 exhibited higher adhesion strength than the others.

3.2 Surface morphologies of MAO coatings

Fig. 3 showed the surface morphologies and EDS profiles of nine different MAO coatings (sample A1–A9). All the samples displayed crater-like and island-like morphologies. The micro-pores' diameters of A3, A6, A9 samples were obviously bigger than the others. And the micro-cracks of A6, A9 were easily observed, which all indicated the addition of NaF increased the occurrence of micro-cracks and size of micro-pores caused by enlarged discharge sparks.[44,45] Most of the micro-pores of samples A2, A3, A4, A7 were filled and sealed with a medley of particles due to the addition of K_2TiF_6. The elements O, Ti, F, Ca, P were detected in these particles due to the absorption of K_2TiF_6 into the discharge channel under high temperature and pressure.[46] Reactions $TiF_6^{2-} + 4OH^- = TiO_2 + 6F^- + 2H_2O$ took place in the discharge channel.[47] Therefore, TiO_2 and fluoride were left in the discharge channel and the pores were sealed. The n-HAp was incorporated into the coatings under strong electric field and absorbed into the pores of the coatings. The existence of C element in the coatings was due to the generated CO_3^{2-} coming from CO_2 atmosphere during MAO treatment. The porosity and pore configuration influenced the corrosion resistance of MAO coatings significantly.[48] The sealed pores and cracks helped to improve the corrosion resistance of samples evidently due to the blocking of corrosive media's access with substrate. Therefore, the addition of n-HAp or K_2TiF_6 generated the self-sealing effects on micro-pores and micro-cracks existing in MAO coatings, as a result, improved the corrosion resistance of the samples.

Cross-sectional morphologies and elemental distribution of samples A3, A4, A5 were shown in Fig. 4. The interface of MAO coatings and the substrate showed a compact and coherent appearance which indicated the good adhesion between MAO coatings and the substrate. The compact inner configuration could effectively prevent the contact of the corrosive medium with the substrate and slow down the corrosion rate. Elements Mg, P, O, F, Ca, Ti were detected in the MAO coatings. The

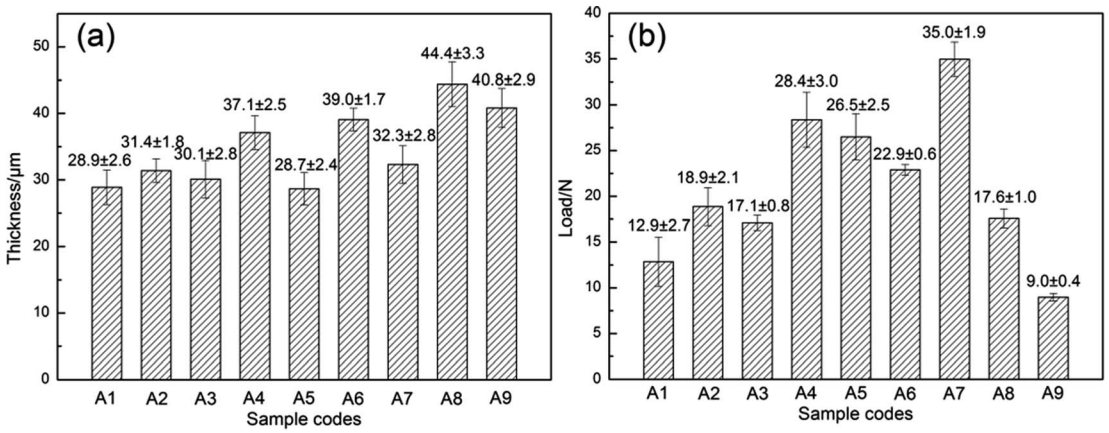

Fig. 2 Thickness (a) and bonding strength (b) of nine different MAO coatings.

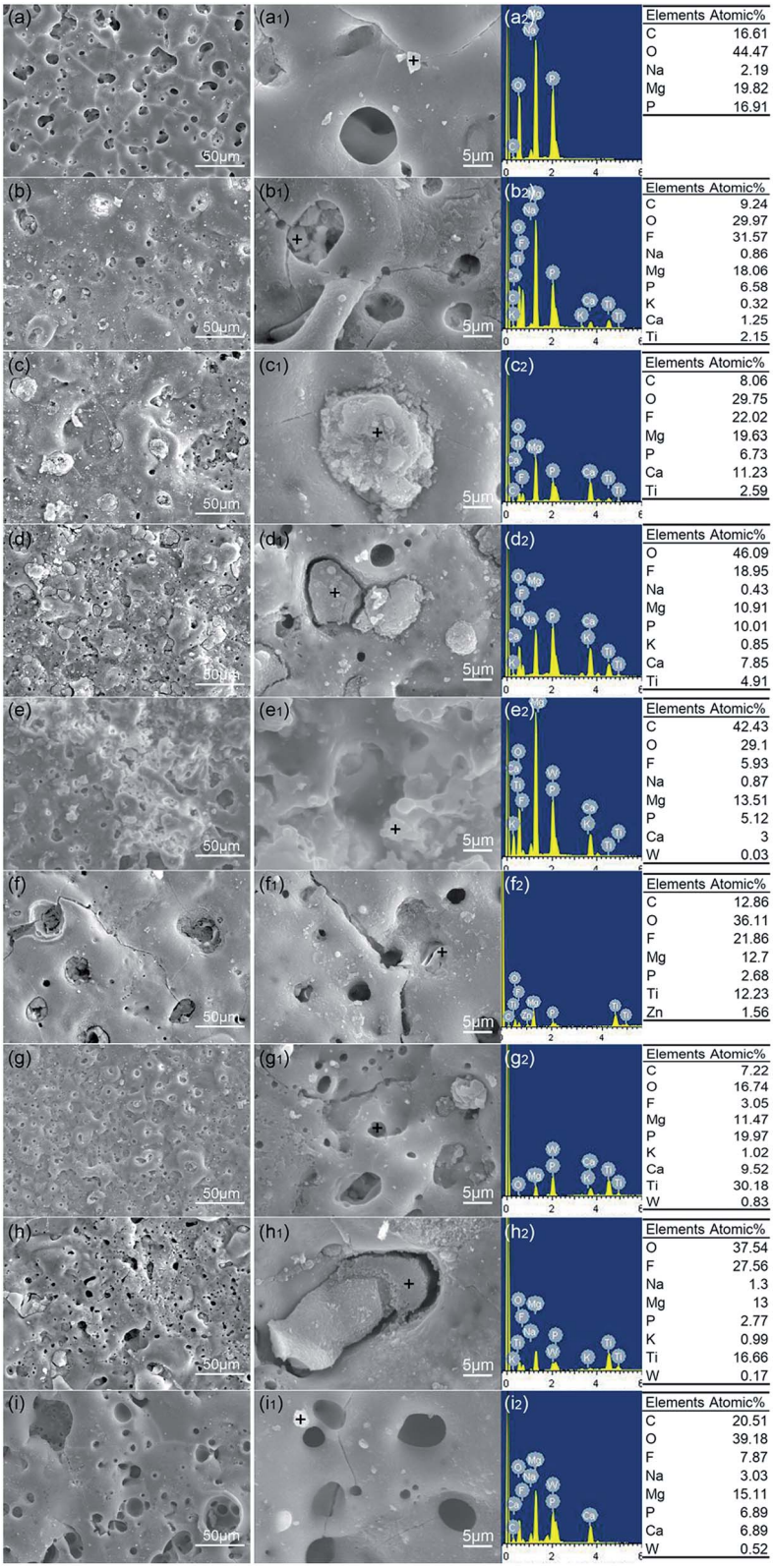

Fig. 3 Surface morphologies and EDS profiles of nine different MAO coatings (a, a_1 and a_2) sample A1, (b, b_1 and b_2) sample A2, (c, c_1 and c_2) sample A3, (d, d_1 and d_2) sample A4, (e, e_1 and e_2) sample A5, (f, f_1 and f_2) sample A6, (g, g_1 and g_2) sample A7, (h, h_1 and h_2) sample A8, (i, i_1 and i_2) sample A9.

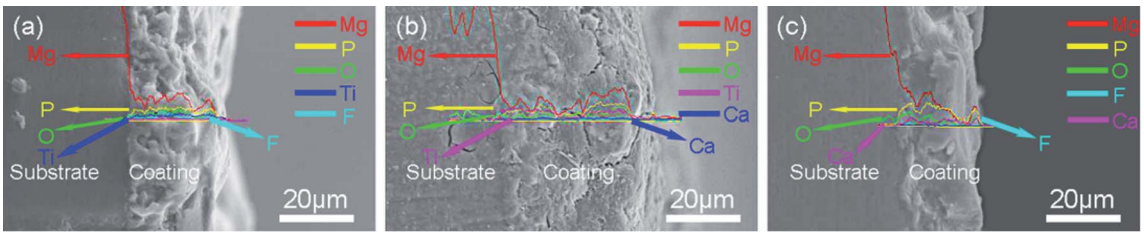

Fig. 4 Cross-sectional morphologies and elemental distribution of samples (a) A3, (b) A4, (c) A5.

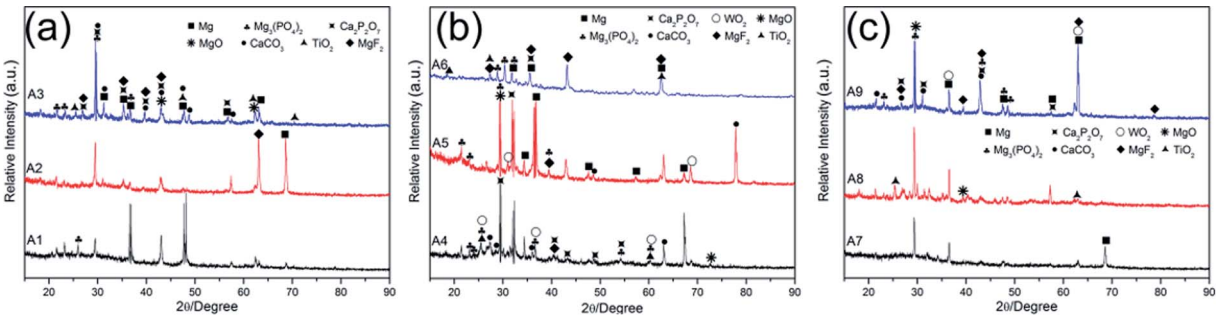

Fig. 5 XRD patterns of MAO coatings prepared by nine different electrolytes (samples A1–A9).

detection of Ca, Ti elements showed the active participation of n-HAp or K_2TiF_6 additives during MAO. Surface morphologies combining with cross-sectional morphologies showed that considerable micro-pores existing in MAO coatings were interconnected. Smaller pores could be observed through the bigger pores from the top layer (as shown in Fig. 3(a_1, b_1 and g_1)).

3.3 Phase composition of MAO coatings

The XRD patterns of MAO coatings prepared by nine different electrolytes (samples A1–A9) were shown in Fig. 5. Metal oxides (MgO, TiO_2, WO_2), fluorides (MgF_2), phosphate ($Mg_3(PO_4)_2$, $Ca_2P_2O_7$), $CaCO_3$ and Mg distributed in nine different MAO coatings. The addition of NaF and K_2TiF_6 led to the formation of MgF_2 phase. And the MgO, MgF_2, $Mg_3(PO_4)_2$ phases were dominant and stable phases that could protect the substrate from corrosion in corrosive environments.[49] The dehydration of $Mg(OH)_2$ led to the formation of MgO. The TiO_2 phase possessed catalytic activity and highly antibacterial properties.[50–52] Furthermore, the free radicals on TiO_2 can induce the formation of apatite that subsequently promoted the adhesion of osteoblast.[53,54] The formation of calcium salts indicated that the incorporation of n-HAp occurred by reactive way during MAO process.[55] Although inert incorporation might take place, the content of the original n-HAp was too minimal to detect.

3.4 Corrosion resistance of MAO coatings

Typical potentiodynamic polarization curves of samples A1–A9 and substrate in SBF were shown in Fig. 6. The corrosion potential (E_{corr}) and corrosion current density (I_{corr}) were also displayed in Fig. 6. Table 3 displayed detailed potentiodynamic polarization data of MAO coated samples. The MAO coatings prevented the direct contact of corrosive ions with the substrate. Therefore, the MAO-treated samples had lower corrosion current density and higher polarization resistance comparing to the bare substrate. The range analysis of orthogonal experiments indicated that the addition of K_2TiF_6 had much more effects on the corrosion resistance of samples than the other additives (as shown in Table 2). The addition of 5 g L^{-1} K_2TiF_6 achieved better corrosion resistance with higher E_{corr} (V *vs.* SCE) and lower I_{corr} (A cm^{-2}). It was due to the addition of K_2TiF_6

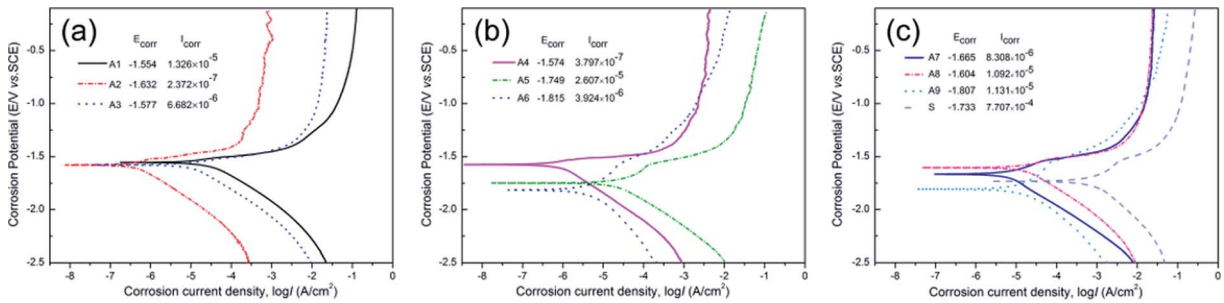

Fig. 6 Potentiodynamic polarization curves of samples A1–A9 and substrate in SBF.

Table 3 Potentiodynamic polarization data of MAO coated samples

Sample codes	I_{corr} (A cm^{-2})	E_{corr} (V *vs.* SCE)	b_a (mV)	b_c (mV)	R_p (Ω cm^2)
A1	1.326×10^{-5}	−1.554	5.376	17.864	1410.9
A2	2.372×10^{-7}	−1.632	8.702	2.456	164261.5
A3	6.682×10^{-6}	−1.577	4.788	18.544	2789
A4	3.797×10^{-7}	−1.574	4.246	27.468	36101.1
A5	2.607×10^{-5}	−1.749	5.236	5.043	1622.3
A6	2.184×10^{-6}	−1.501	4.574	7.043	17134.2
A7	8.308×10^{-6}	−1.665	4.052	7.006	4732.7
A8	1.092×10^{-5}	−1.604	4.637	19.209	1669.2
A9	1.131×10^{-5}	−1.807	5.844	4.796	3613.4
S	7.707×10^{-4}	−1.733	4.596	4.939	59.2

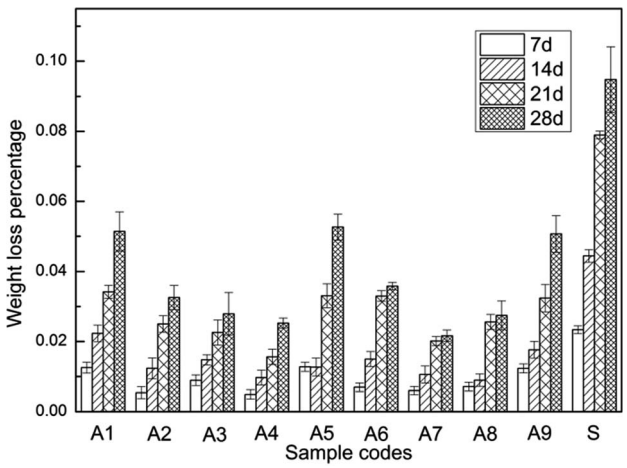

Fig. 7 Weight loss percentage of samples A1–A9 and substrate immersed in SBF for 7, 14, 21, 28 days respectively.

promoted the formation of MgF_2 phases, which acted as a barrier to protect the substrate from being further corroded.[56] The addition of K_2TiF_6 helped to improve the corrosion resistance of samples, which was in accordance with the observation and deduction of surface morphologies of MAO coatings above. Adding n-HAp also evidently improved the corrosion resistance of the samples, and the concentration of 5 g L^{-1} brought the best effects. But the addition of Na_2WO_4 and NaF had no obvious impact on the corrosion properties of the samples.

The weight loss percentage of samples A1–A9 and substrate immersed in SBF for 7, 14, 21, 28 days was shown in Fig. 7. Comparing to the substrate, the weight loss percentage of A1–A9 samples was obviously lower, which proved the superior corrosion resistance of MAO coatings. After 28 days of immersion, samples without the addition of K_2TiF_6 (A1, A5, A9) corroded more severely than the other samples. The data in Table 2 showed that the increase of K_2TiF_6 could retard the corrosion rate of samples markedly. The addition of n-HAp also helped to reduce the degradation rate. However, the increase of NaF additives impaired the corrosion resistance of samples due to more micro-cracks and larger micro-pores caused by enlarged discharge sparks.

3.5 Coating biocompatibility

Fig. 8 showed the pH values of samples A1–A9 and substrate immersed in SBF for 28 days. MAO coatings helped to decrease the pH values during the degradation process comparing to the substrate. Liu *et al.*[57] demonstrated that the weak alkaline physiological environment promoted the differentiation of osteoblasts while inhibited the formation of osteoclast. And the weak alkaline condition accelerated the repairing process of the damaged bones. As shown in Fig. 8, the pH values of A2, A4, A7 samples were steady and ranged from 7.32–7.65, 6.91–7.58, 7.18–7.65 respectively, which was close to the physiological environment. Shen *et al.*[58] proved that the optimal pH values for the viability of osteoblast ranged from 8 to 8.5. The pH values of the substrate ranged from 7.88 to 8.62. Therefore, even though the MAO coatings would degrade, the exposed substrate could offer a favorable environment for the growth of the osteoblast.

The surface morphologies and elemental composition of samples A1–A9 and substrate after immersed in SBF for 28 days were shown in Fig. 9. Typical spherical clusters with honeycomb like constructions appeared on the surface of A1 and A5 samples. In addition, numerous spherical, lamellar and blocky particles with different size generated on the surface of samples A1–A9 and substrate after the immersion. The elements C, O, Ca, P, F, Mg, Cl, Ti were detected in the particles or surface of samples. The elemental composition of samples A1–A9 and substrate atomic percentage and molar ratio of Ca and P on the surface of samples A1–A9 and substrate was shown in Table 4. It indicated that the

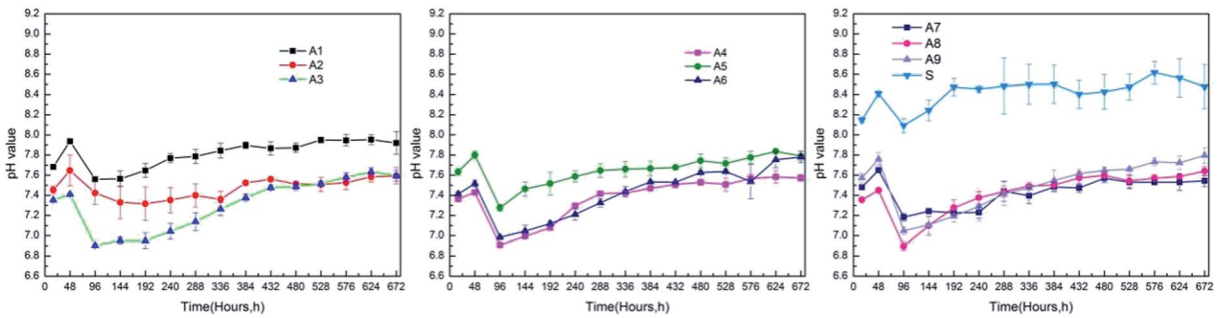

Fig. 8 pH values of samples A1–A9 and substrate immersed in SBF for 28 days.

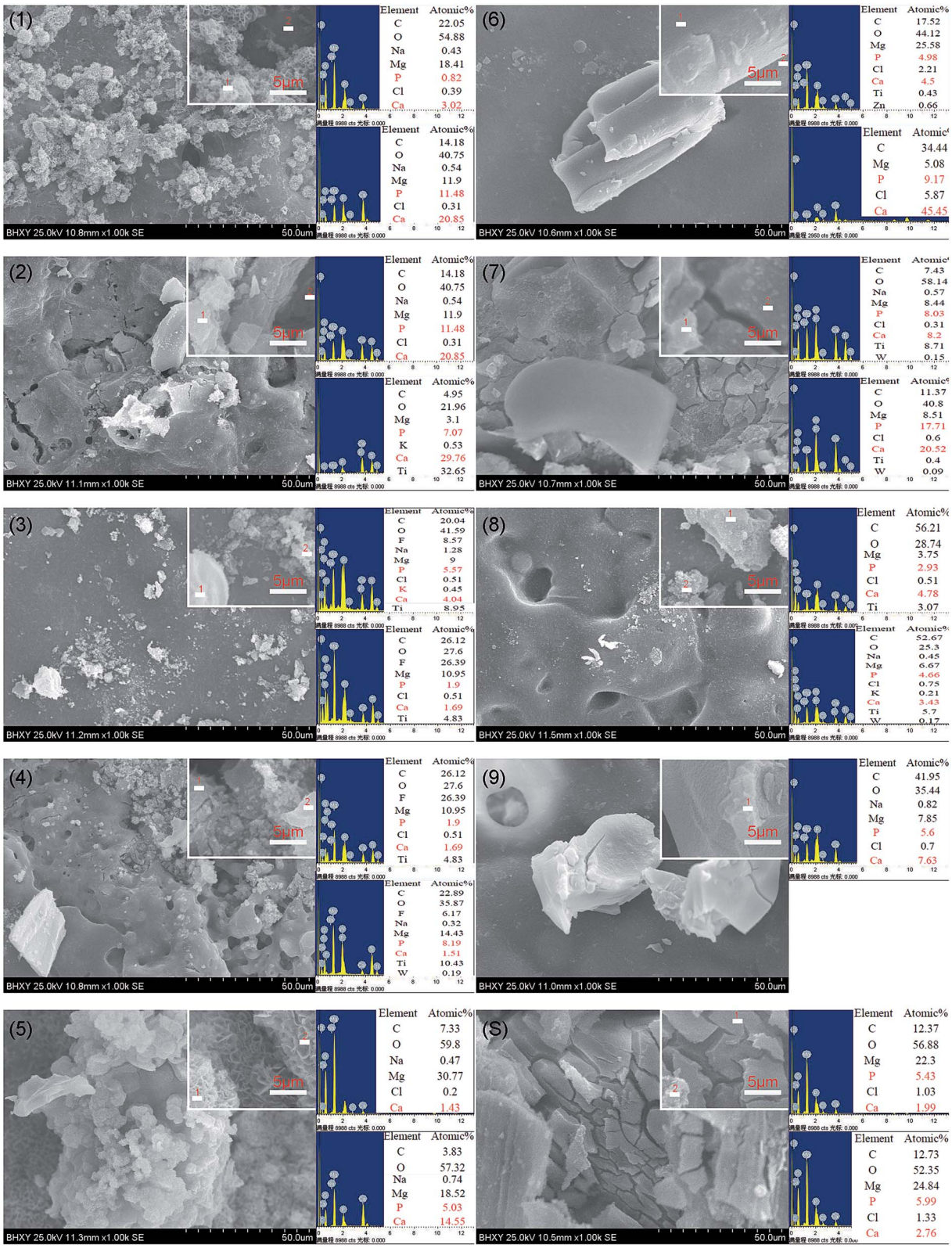

Fig. 9 Surface morphologies and elemental composition of samples A1–A9 and substrate after immersed in SBF for 28 days.

proportion of Ca and P in some of the new generated products was pretty high, which demonstrated the surfaces' ability of inducing the precipitation of calcium phosphates. The results indicated that samples with and without MAO coatings all possessed excellent biocompatibility and bioactivity.

The XRD patterns of samples A1–A9 and substrate immersed in SBF for 28 days were shown in Fig. 10. The

Table 4 The atomic percentage and molar ratio of Ca and P on the surface of samples A1–A9 and substrate

Sample codes	A1-1	A1-2	A2-1	A2-2	A3-1	A3-2	A4-1	A4-2	A5-1	A5-2
Ca (atomic%)	3.02	20.85	8.48	29.76	4.04	1.69	3.82	1.51	1.43	14.55
P (atomic%)	0.82	11.48	7.15	7.07	5.57	1.9	3.12	8.19	—	5.03
Ca/P	3.68	1.82	1.19	4.21	0.73	0.89	1.22	0.18	—	2.89

Sample codes	A6-1	A6-2	A7-1	A7-2	A8-1	A8-2	A9-1	S-1	S-2
Ca (atomic%)	4.5	45.45	3.02	20.52	4.78	3.43	7.63	12.2	16.11
P (atomic%)	4.98	9.17	0.82	17.71	2.93	4.66	5.6	10.66	13.97
Ca/P	0.90	4.96	3.68	1.16	1.63	0.74	1.36	1.14	1.15

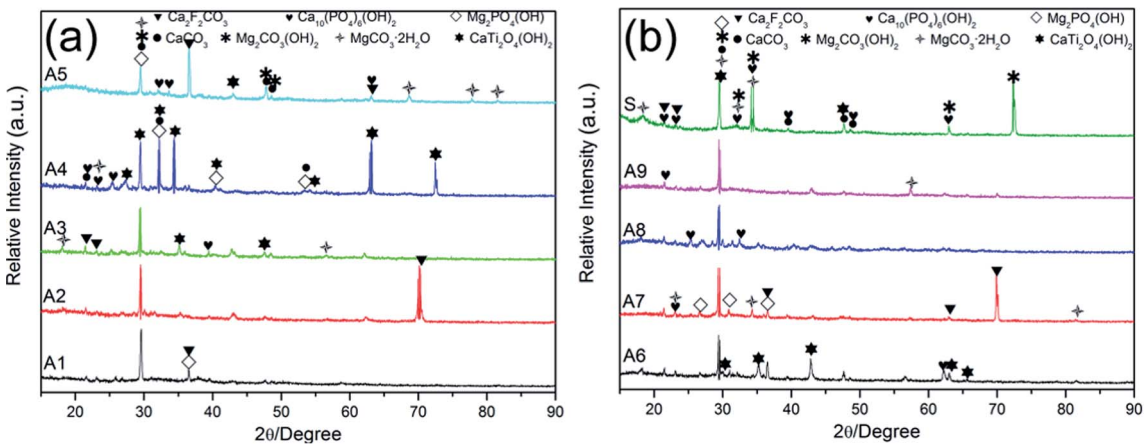

Fig. 10 XRD patterns of samples A1–A9 and substrate immersed in SBF for 28 days.

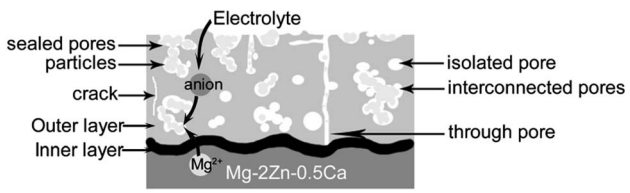

Fig. 11 Schematic cross-sectional illustrations of MAO coatings on the Mg–2Zn–0.5Ca substrate.

abundant existence of Cl^- in SBF accelerated the pitting corrosion of samples, but the presence of HPO_4^{2-}/PO_4^{2-}, HCO_3^-/CO_3^{2-}, Ca^{2+} contributed to the formation and precipitation of calcium phosphate and carbonate salt which may seal the micro-pores and prevent further corrosion of the samples.[1,59,60] Hydroxyapatite ($Ca_{10}(PO_4)_6(OH)_2$) was detected in the immersed samples which demonstrated the excellent biocompatibility of these MAO coated samples.

3.6 Growth mechanism of MAO coatings

The electrolytes composition of samples A4 and A7 were relatively close to the optimal combination. It could be observed that white bumps distributed unevenly on samples A4 and A7 (as shown in Fig. 1 (A4, A7)). On the contrary, the micro-morphologies of samples A4 and A7 showed that the micro-pores distributed uniformly on the MAO coatings. The micro-pores of samples A4 and A7 were small and almost the same size. Furthermore, almost all the micro-pores and micro-cracks were sealed by different particles (as shown in Fig. 3(A4 and A7)). Without the addition of NaF, the MAO coatings of samples A4 and A7 were relatively thin, but the adhesion and corrosion resistance of samples A4 and A7 was excellent. The steady pH values during the immersion in SBF as well as the calcium phosphate generated on MAO coatings after immersion all demonstrated the fabulous biocompatibility of samples A4 and A7.

Fig. 11 showed the schematic cross-sectional illustrations of MAO coatings on the Mg–2Zn–0.5Ca substrate which was summarized by surface and cross-sectional morphologies of MAO coatings. The interface of the substrate and MAO coatings presented a wavy-jagged and integrated appearance. Electrochemical reactions, plasma electrolysis reactions and thermal diffusion went on simultaneously during the process of coating growth.[61,62] First, in the stage of high pressure anodization, a compact and uniform inner layer grew promptly to 1.7 ± 0.6 μm by ion migration.[63] As the substrate was been covered by insulated oxide coatings, the voltage increased rapidly and exceeded the breakdown threshold which leads to electron avalanches. The electrons attaching to the gas bubbles triggered off plasma activities.[64] The microscopic localized plasma discharge broke the coating and generated numerous discharge channels, with the potential to impair the corrosion resistance of coatings.[60] And the micro-pores formed by plasma discharges were more

vulnerable for next electron avalanches on account of its lower breakdown voltage.[65] This was reflected as a great deal of small sparks moving rapidly and circuitously over the surface of the sample. Therefore, a series of interconnected pores formed in the coating of the sample. In the following stage, the coating grew tougher to break, the voltage increased slower and the sparks grew more intensive and extended. The more concentrated discharges caused the formation of through pores which might jeopardize the corrosion resistance of the coatings.[61] But the plasma discharge locating at the coating/electrolyte interface induced the deposition of electrolyte composition in the inner discharge channel. Therefore, the micro-pores existing in surface coatings were partially self-sealed by electrolyte deposition combing with migration of Mg^{2+} from the substrate.[66,67] In addition, the sediments formed in micro-pores were unconsolidated instead of an integral chunk (as shown in Fig. 3), the phase composition was complex after a series of "breakdown–melting–ion migration–deposition". The formation of micro-cracks attributed to two reasons: one was the lattice distortion among the hexagonal closet-packed (HCP) lattice of Mg and various crystal structures of different phases generated in the coatings, led to the internal stress differential; the other was the Pilling–Bedworth ratios (PBR) of the oxides, fluorides, phosphates, carbonates exiting in coatings were different.[60] These mismatches led to the formation of micro-cracks which impaired the corrosion resistance of the coatings.

4 Conclusion

Nine different micro-arc oxidation coatings with different colors were fabricated on Mg–2Zn–0.5Ca alloys to improve the mechanical properties, corrosion resistance and biocompatibility of the magnesium alloy substrate. The following conclusions can be drawn:

(1) The addition of 0.5 g L^{-1} Na_2WO_4 markedly elevated the bonding strength of the coatings with the substrate. Additives n-HAp participated in the MAO process and improved the adhesion strength of the coatings with the substrate. The participation of n-HAp helped the self-sealing of the coatings and enhanced the corrosion resistance of the samples.

(2) The addition of K_2TiF_6 promoted the formation of MgF_2 phase and increased the thickness of the coatings. The MgF_2 phase combining with Ti element led to the blue color of MAO coatings. The corrosion resistance of the samples was significantly improved due to the sealing effects of K_2TiF_6 additives on the micro-pores and micro-cracks in MAO coatings.

(3) The addition of NaF increased the thickness of the coatings, whilst increased the occurrence of micro-cracks and enlarged the micro-pores on account of enlarged discharge sparks. Therefore, the samples with NaF additives possessed lower corrosion resistance than the other samples.

(4) Large amount of micro-pores formed in MAO coatings were interconnected. The A4, A7 samples exhibited the best performance in terms of mechanical properties, corrosion resistance and biocompatibility. According to the orthogonal experiments, the optimal combination of additives is: 0.5 g L^{-1} Na $_2WO_4$, 0 g L^{-1} NaF, 5 g L^{-1} n-HAp, 5 g L^{-1} K_2TiF_6, considering good mechanical properties, corrosion resistance and biocompatibility.

Data availability statement

All relevant data are within the paper.

Conflicts of interest

The authors declare that they have no competing interests.

Acknowledgements

This work was financially supported by the Key R&D Project of Shandong Province (Grant no. 2018CXGC0811), China Postdoctoral Science Foundation Funded Project (Grant no. 2019M652184) and China Postdoctoral Science Foundation Special Funded Project (Grant no. 2019T120589).

References

1 S. Agarwal, J. Curtin, B. Duffy and S. Jaiswal, *Mater. Sci. Eng., C*, 2016, **68**, 948–963.
2 H. Tang, Y. Han, T. Wu, W. Tao, X. Jian, Y. Wu and F. Xu, *Appl. Surf. Sci.*, 2017, **400**, 391–404.
3 M. Carboneras, M. C. García-Alonso and M. L. Escudero, *Corros. Sci.*, 2011, **53**, 1433–1439.
4 H. Ma, Y. Gu, S. Liu, J. Che and D. Yang, *Surf. Coat. Technol.*, 2017, **331**, 179–188.
5 Y. Xin, K. Huo, H. Tao, G. Tang and P. K. Chu, *Acta Biomater.*, 2008, **4**, 2008–2015.
6 S. Durdu and M. Usta, *Appl. Surf. Sci.*, 2012, **261**, 774–782.
7 F. Witte, J. Fischer, J. Nellesen, H. Crostack, V. Kaese, A. Pisch, F. Beckmann and H. Windhagen, *Biomaterials*, 2006, **27**, 1013–1018.
8 Y. Pan, S. He, D. Wang, D. Huang, T. Zheng, S. Wang, P. Dong and C. Chen, *Mater. Sci. Eng., C*, 2015, **47**, 85–96.
9 J. Fischer, M. H. Prosenc, M. Wolff, N. Hort, R. Willumeit and F. Feyerabend, *Acta Biomater.*, 2010, **6**, 1813–1823.
10 B. A. Shaw, *Corrosion Resistance of Magnesium Alloys*, ASM International, 2003, vol. 13, pp. 692–696.
11 X. Gu, Y. Zheng, Y. Cheng, S. Zhong and T. Xi, *Biomaterials*, 2009, **30**, 484–498.
12 S. Cai, T. Lei, N. Li and F. Feng, *Mater. Sci. Eng., C*, 2012, **32**, 2570–2577.
13 M. Yamaguchi, *J. Trace Elem. Exp. Med.*, 1998, **11**, 119–135.
14 G. Jin, H. Qin, H. Cao, S. Qian, Y. Zhao, X. Peng, X. Zhang, X. Liu and P. K. Chu, *Biomaterials*, 2014, **35**, 7699–7713.
15 W. L. Yu, D. Y. Chen, Z. Y. Ding, M. Qiu, Z. Zhang, J. Shen, X. Zhang, S. Zhang, Y. He and Z. Shi, *RSC Adv.*, 2016, **6**, 45219–45230.
16 G. Jin, H. Qin, H. Cao, Y. Qiao, Y. Zhao, X. Peng, X. Zhang, X. Liu and P. K. Chu, *Biomaterials*, 2015, **65**, 22–31.
17 M. B. Kannan and R. K. S. Raman, *Biomaterials*, 2008, **29**, 2306–2314.
18 G. Wu, Y. Fan, H. Gao, C. Zhai and Y. P. Zhu, *Mater. Sci. Eng., A*, 2005, **408**, 255–263.

19 D. Zander and N. A. Zumdick, *Corros. Sci.*, 2015, **93**, 222–233.
20 Y. Lu, A. R. Bradshaw, Y. L. Chiu and I. P. Jones, *Mater. Sci. Eng., C*, 2015, **48**, 480–486.
21 B. Zhang, Y. Hou, X. Wang, Y. Wang and L. Geng, *Mater. Sci. Eng., C*, 2011, **31**, 1667–1673.
22 N. Nashrah, M. P. Kamil, D. K. Yoon, Y. G. Kim and Y. G. Ko, *Appl. Surf. Sci.*, 2019, **497**, 143772.
23 Y. Li, Y. Guan, Z. Zhang and S. Ynag, *Appl. Surf. Sci.*, 2019, **478**, 866–871.
24 Q. Du, D. Wei, S. Wang, S. Cheng, Y. Wang, B. Li, D. Jia and Y. Zhou, *Appl. Surf. Sci.*, 2019, **487**, 708–718.
25 D. Luo, Y. Liu, X. Yin, H. Wang, Z. Han and L. Ren, *J. Alloys Compd.*, 2018, **731**, 731–738.
26 H. F. Guo, M. Z. An, H. B. Huo, S. Xu and L. J. Wu, *Appl. Surf. Sci.*, 2006, **252**, 7911–7916.
27 R. Zhou, D. Wei, H. Yang, S. Cheng, W. Feng, B. Li, Y. Wang, D. Jia and Y. Zhou, *J. Mater. Sci.: Mater. Med.*, 2014, **25**, 1307–1318.
28 Y. K. Pan, C. Z. Chen, D. G. Wang and T. G. Zhao, *Colloids Surf., B*, 2013, **109**, 1–9.
29 L. Xu, C. Wu, X. Lei, K. Zhang, C. Liu, J. Ding and X. Shi, *Surf. Coat. Technol.*, 2018, **342**, 12–22.
30 Y. Jang, Z. Tan, C. Jurey, Z. Xu, Z. Dong, B. Collins, Y. Yun and J. Sankar, *Mater. Sci. Eng., C*, 2015, **48**, 28–40.
31 H. Tang, Y. Han, T. Wu, W. Tao, X. Jian, Y. Wu and F. Xu, *Appl. Surf. Sci.*, 2017, **400**, 391–404.
32 F. Zhao, A. Liao, R. Zhang, S. Zhang, H. Wang, X. Shi, M. Li and X. He, *Trans. Nonferrous Met. Soc. China*, 2010, **20**, s683–s687.
33 L. Lei, L. Li, L. Zhang, D. Chen and W. Tian, *Polym. Degrad. Stab.*, 2009, **94**, 1494–1502.
34 S. Chen, J. Tu, Q. Hu, X. Xiong, J. Wu, J. Zou and X. Zeng, *J. Non-Cryst. Solids*, 2017, **456**, 125–131.
35 A. R. Ribeiro, F. Oliveira, L. C. Boldrini, P. E. Leite, P. Falagan-Lotsch, A. B. R. Linhares, W. F. Zambuzzi, B. Fragneaud, A. P. C. Campos, C. P. Gouvêa, B. S. Archanjo, C. A. Achete, E. Marcantonio, L. A. Rocha and J. M. Granjeiro, *Mater. Sci. Eng., C*, 2015, **54**, 196–206.
36 L. Song, Y. Kou, Y. Song, D. Shan, G. Zhu and E. H. Han, *Mater. Corros.*, 2011, **62**, 1124–1132.
37 W. Yang, J. Wang, D. Xu, J. Li and T. Chen, *Surf. Coat. Technol.*, 2015, **283**, 281–285.
38 M. Tang, G. Li, W. Li, H. Liu and L. Zhu, *J. Alloys Compd.*, 2013, **562**, 84–89.
39 Y. H. Xia, B. P. Zhang, C. X. Lu and L. Geng, *Mater. Sci. Eng., C*, 2013, **33**, 5044–5050.
40 X. Wu and D. Y. C. Leung, *Appl. Energy*, 2011, **88**, 3615–3624.
41 H. Li, H. Guan, P. Han, Y. Li and C. Zhang, *Opt. Commun.*, 2013, **287**, 162–166.
42 H. Tang, Y. Han, T. Wu, W. Tao, X. Jian, Y. Wu and F. Xu, *Appl. Surf. Sci.*, 2017, **400**, 391–404.
43 M. Tang, Z. Feng, G. Li, Z. Zhang and R. Zhang, *Surf. Coat. Technol.*, 2015, **264**, 105–113.
44 H. Chen, G. Lv, G. Zhang, H. Pang, X. Wang, H. Lee and S. Yang, *Surf. Coat. Technol.*, 2010, **205**, S32–S35.
45 L. Zhang, J. Zhang, C. Chen and Y. Gu, *Corros. Sci.*, 2015, **91**, 7–28.
46 W. Yang, D. Xu, Q. Guo, T. Chen and J. Chen, *Surf. Coat. Technol.*, 2018, **349**, 522–528.
47 X. Lin, X. Wang, L. Tan, P. Wan, X. Yu, Q. Li and K. Yang, *Ceram. Int.*, 2014, **40**, 10043–10051.
48 L. Zhang, J. Zhang, C. Chen and Y. Gu, *Corros. Sci.*, 2015, **91**, 7–28.
49 H. Duan, C. Yan and F. Wang, *Electrochim. Acta*, 2007, **52**, 3785–3793.
50 B. Arora, B. Arora, M. Murar and V. Dhumale, *J. Exp. Nanosci.*, 2015, **10**, 819–827.
51 R. Michal, E. Dworniczek, M. Caplovicova, O. Monfort, P. Lianos, L. Caplovic and G. Plesch, *Appl. Surf. Sci.*, 2016, **371**, 538–546.
52 C. Chung, H. Lin, C. Chou, P. Hsieh, C. Hsiao, Z. Shi and J. He, *Surf. Coat. Technol.*, 2009, **203**, 1081–1085.
53 T. Yang, H. Shu, H. Chen, C. Chung and J. He, *Surf. Coat. Technol.*, 2014, **259**, 185–192.
54 C. M. Lin and S. K. Yen, *Mater. Sci. Eng., C*, 2006, **26**, 54–64.
55 X. Lu, C. Blawert, Y. Huang, H. Ovri, M. L. Zheludkevich and K. U. Kainer, *Electrochim. Acta*, 2016, **187**, 20–33.
56 L. Rama Krishna and G. Sundararajan, *JOM*, 2014, **66**, 1045–1060.
57 W. Liu, T. Wang, C. Yang, B. W. Darvell, J. Wu, K. Lin, J. Chang, H. Pan and W. W. Lu, *Osteoporosis Int.*, 2016, **27**, 93–104.
58 Y. Shen, W. Liu, C. Wen, H. Pan, T. Wang, B. W. Darvell, W. W. Lubc and A. W. Huange, *J. Mater. Chem.*, 2012, **22**, 8662.
59 M. B. Kannan, R. K. Singh Raman, F. Witte, C. Blawert and W. Dietzel, *J. Biomed. Mater. Res., Part B*, 2011, **96B**, 303–309.
60 L. Cui, R. Zeng, S. Guan, W. Qi, F. Zhang, S. Li and E. Han, *J. Alloys Compd.*, 2017, **695**, 2464–2476.
61 R. O. Hussein, X. Nie and D. O. Northwood, *Electrochim. Acta*, 2013, **112**, 111–119.
62 R. O. Hussein, X. Nie, D. O. Northwood, A. Yerokhin and A. Matthews, *J. Phys. D: Appl. Phys.*, 2010, **43**, 105203.
63 D. Veys-Renaux, E. Rocca and G. Henrion, *Electrochem. Commun.*, 2013, **31**, 42–45.
64 M. P. Kamil, M. Kaseem, Y. H. Lee and Y. G. Ko, *J. Alloys Compd.*, 2017, **707**, 167–171.
65 H. Nasiri Vatan, R. Ebrahimi-kahrizsangi and M. Kasiri-asgarani, *J. Alloys Compd.*, 2016, **683**, 241–255.
66 L. Zhu, X. Ke, B. Zhang, Y. Zhang and M. Sui, *J. Alloys Compd.*, 2018, **766**, 88–94.
67 L. Zhu, Z. Guo, Y. Zhang, Z. Li and M. Sui, *Electrochim. Acta*, 2016, **208**, 296–303.

